Mon. Not. R. Astron. Soc. **312**, 166–176 (2000)

The supergalactic plane revisited with the Optical Redshift Survey

O. Lahav,[1,2]★ B. X. Santiago,[3] A. M. Webster,[1] Michael A. Strauss,[4]† M. Davis,[5] A. Dressler[6] and J. P. Huchra[7]

[1]*Institute of Astronomy, Madingley Road, Cambridge CB3 0HA*
[2]*Racah Institute of Physics, The Hebrew University, Jerusalem 91904, Israel*
[3]*Instituto de Física, Universidade Federal do Rio Grande do Sul, 91501-970, Porto Alegre, RS, Brazil*
[4]*Princeton University Observatory, Princeton, NJ 08544, USA*
[5]*Physics and Astronomy Departments, University of California, Berkeley, CA 94720, USA*
[6]*Observatories of the Carnegie Institution, 813 Santa Barbara St, Pasadena, CA 91101, USA*
[7]*Center for Astrophysics, 60 Garden St, Cambridge, MA 02138, USA*

Accepted 1999 September 20. Received 1999 September 6; in original form 1998 October 5

ABSTRACT

We re-examine the existence and extent of the planar structure in the local galaxy density field, the so-called supergalactic plane (SGP). This structure is studied here in three dimensions using both the new Optical Redshift Survey (ORS) and the *IRAS* 1.2-Jy redshift survey. The density contrast in a slab of thickness $20\,h^{-1}$ Mpc and diameter 80 Mpc aligned with the standard de Vaucouleurs supergalactic coordinates is $\delta_{\rm sgp} \sim 0.5$ for both ORS and *IRAS*. The structure of the SGP is not well described by a homogeneous ellipsoid, although it does appear to be a flattened structure, which we quantify by calculating the moment of inertia tensor of the density field. The directions of the principal axes vary with radius, but the minor axis remains within $\theta_z \sim 30^\circ$ of the standard SGP *Z*-axis, out to a radius of $80\,h^{-1}$ Mpc, for both ORS and *IRAS*. However, the structure changes shape with radius, varying between a flattened pancake and a dumbbell, the latter at a radius of $\sim 50\,h^{-1}$ Mpc, where the Great Attractor and Perseus–Pisces superclusters dominate the distribution. This calls to question the connectivity of the 'plane' beyond $\sim 40\,h^{-1}$ Mpc. The configuration found here can be viewed as part of a web of filaments and sheets, rather than as an isolated pancake-like structure. An optimal minimum variance reconstruction of the density field using Wiener filtering, which corrects for both redshift distortion and shot noise, yields a similar misalignment angle and behaviour of axes. The background-independent statistic of axes proposed here can be best used for testing cosmological models by comparison with *N*-body simulations.

Key words: methods: statistical – galaxies: distances and redshifts – large-scale structure of Universe.

1 INTRODUCTION

The major planar structure in the local universe, the supergalactic plane (SGP), was recognized by de Vaucouleurs (1953, 1956, 1958, 1975a,b) using the Shapley–Ames catalogue, following an earlier analysis of radial velocities of nearby galaxies, which suggested a differential rotation of the 'metagalaxy' by Rubin (1951). This remarkable feature in the distribution of nebulae was in fact already noticed by William Herschel more than 200 years earlier (for historical reviews see Flin 1986, Rubin 1989).

When referring to the SGP in this paper we mean the planar structure in the galaxy distribution. This should be distinguished from the formal definition of supergalactic coordinates. de Vaucouleurs, de Vaucouleurs & Corwin (1976) and de Vaucouleurs et al. (1991) defined a spherical-coordinate system *SGL*, *SGB* in which the equator roughly lies along the SGP (as identified at the time), with the North Pole ($SGB = 90^\circ$) in the direction of Galactic coordinates ($l = 47.37^\circ$; $b = +6.32^\circ$). The position $SGL = 0^\circ$, $SGB = 0^\circ$ is at ($l = 137.37^\circ$, $b = 0^\circ$), which is one of the two regions where the SGP is crossed by the Galactic plane. The Virgo cluster lies in the direction ($SGL = 104^\circ$; $SGB = -2^\circ$). Traditionally, the Virgo cluster was regarded as the centre of an overdense region called the 'Local Supercluster' (e.g. Davis & Huchra 1982; Hoffman & Salpeter 1982; Tully & Shaya 1984; Lilje, Yahil & Jones 1986). However, some of the much larger superclusters that are seen in recent redshift surveys, such as the

★ E-mail: lahav@ast.cam.ac.uk
† Alfred P. Sloan Foundation Fellow, and Cottrell Fellow of Research Corporation.

Great Attractor and Perseus–Pisces, are near the SGP, and are possibly connected with the Local Supercluster, in the sense of being simply connected by an isodensity contour above the mean density (cf. Strauss et al. 1992; Strauss & Willick 1995; Santiago et al. 1995).

Although the SGP is clearly visible in whole-sky galaxy catalogues (e.g. Lynden-Bell & Lahav 1988; Lynden-Bell et al. 1988; Raychaudhury 1989; see also the references above), the extent of planar structure in the galaxy distribution in three dimensions has seen little quantitative examination in recent years. Tully (1986, 1987) claimed that the flattened distribution of clusters extends across a diameter of $\sim 0.1c$ with axial ratios of 4:2:1. Shaver & Pierre (1989) found that radio galaxies are more strongly concentrated to the SGP than optical galaxies are, and that the SGP as represented by radio galaxies extends out to redshift $z \sim 0.02$. Stanev et al. (1995) claimed that energetic cosmic rays arrive preferentially from the direction of the SGP, where potential sources (e.g. radio galaxies) are concentrated, but this result was criticized by Waxman, Fisher & Piran (1997). Di Nella & Paturel (1995) revisited the SGP using a compilation of nearly 5700 galaxies larger than 1.6 arcmin, and found indeed that galaxies were concentrated close to the SGP. Loan (1997) and Baleisis et al. (1998) searched for the SGP in projection in the 87GB (north) and PMN (south) radio surveys, and found signatures at the 1σ and 3σ levels, respectively.

The existence of a pancake-like structure has important theoretical implications. Gravity amplifies deviations from sphericity; an initial oblate homogeneous ellipsoid evolves into a disc, and an initial prolate structure ends up as a spindle (Lin, Mestel & Shu 1965). White & Silk (1979) modelled the Local Supercluster as a homogeneous ellipsoid in an expanding universe, and considered implications for cosmological models and initial conditions. Although such a simple model is insightful, the structure of the SGP is far more complicated than a homogeneous ellipsoid, as we show below. In a more realistic cosmological scenario, where the primordial density field is Gaussian, non-spherical shapes are more abundant than spherical ones (Doroshkevich 1970; Bardeen et al. 1986), and hence are expected to appear at the present epoch as even more non-spherical. In the context of the 'top-down' hot dark matter scenario, Zel'dovich (1970) showed that pancake-like structures are the natural outcome of gravitational instability in the quasi-linear regime. Further studies have indicated that a web of filaments could also form in hierarchical cold dark matter (bottom-up) scenarios (e.g. Bond, Kofman & Pogosyan 1996), but the shapes look quite different in different scenarios, as a result of both initial conditions and the cosmic time, which allows the perturbations to grow. Hence, quantitative measures of the shape of the SGP and other observed filamentary structures and superclusters (Bahcall 1988) could be very important in distinguishing between models, e.g. by applying the measure to both data and to *N*-body simulations.

Here we study the properties of the SGP using the Optical Redshift Survey (ORS, Santiago et al. 1995), which provides the most detailed and uniform optically selected sample of the local galaxy density field to date. For comparison, we also use the full-sky redshift survey of galaxies selected from the data base of the *Infrared Astronomical Satellite* (*IRAS*), complete to 1.2 Jy at 60 μm (Fisher et al. 1995a). In this paper we calculate the 'moment of inertia' (MoI) of the density field to quantify the shape of the SGP (cf. Babul & Starkman 1992; Luo & Vishniac 1995; Dave et al. 1997; Sathyaprakash et al. 1998).

The outline of the paper is as follows. Section 2 describes the ORS and *IRAS* samples, while in Section 3 we discuss the visual impression and preliminary analysis of the SGP. Section 4 describes the MoI formalism; we also develop related statistics that are independent of the background determination. Section 5 gives the MoI results when applied to the observational samples, and Section 6 presents Wiener reconstruction of the MoI for *IRAS*. Section 7 gives interpretation of the results using mock realizations, and conclusions and future work are discussed in Section 8.

2 THE ORS AND *IRAS* SAMPLES

The Optical Redshift Survey (ORS, Santiago et al. 1995) covers the sky at Galactic latitude $|b| > 20°$. The survey was drawn from the UGC (Nilson 1973), ESO (Lauberts 1982), and ESGC (Corwin & Skiff 1995) galaxy catalogues, and contains two subsets: one complete to a blue photographic magnitude of 14.5, and the other complete to a blue major diameter of 1.9 arcmin. The entire sample consists of 8457 galaxies, with redshifts available for 98 per cent of them; ≈1300 new redshifts were measured to complete the survey. The high number density of galaxies in ORS makes it ideal for cosmographical studies of the local universe.

As ORS only covers $|b| > 20°$, we filled in the zone of avoidance (ZOA) at $|b| < 20°$ with galaxies from the *IRAS* 1.2-Jy survey (Fisher et al. 1995a). The zone of avoidance in *IRAS*, $|b| < 5°$, was filled by interpolation based on the observed galaxy distribution below and above the ZOA (Yahil et al. 1991). While in principle it is possible to interpolate over the ORS ZOA, e.g. by hand or using a Wiener reconstruction (Lahav et al. 1994), we prefer to include real structure as probed by *IRAS* even at the price of mixing two different data sets. Hereafter, when we refer to the ORS sample, we mean that supplemented by the *IRAS* 1.2-Jy galaxies at $|b| < 20°$.

Owing to Galactic extinction and the diversity of catalogues used, the selection function of ORS depends on both distance and direction (Santiago et al. 1996). In order to account for these selection effects, we associate a weight with each galaxy. For a uniform survey like *IRAS* (see below) the selection function ϕ depends only on the distance to a galaxy, $|\boldsymbol{x}|$, and hence the weight is simply

$$w_{\rm gal} = \frac{1}{\langle n\rangle \phi(|\boldsymbol{x}|)}, \tag{1}$$

where the mean number density of galaxies is estimated by

$$\langle n\rangle = \frac{1}{V}\sum_{\rm gal} 1/\phi(|\boldsymbol{x}|), \tag{2}$$

where V is the volume surveyed.

For ORS, we follow Santiago et al. (1996) and Hermit et al. (1996) and weight each galaxy by:

$$w_{\rm gal} = \frac{1}{\langle n\rangle_\mu \phi(\boldsymbol{x})}\frac{\langle n\rangle_{\mu,\,IRAS}}{\langle n\rangle_{\rm tot,\,IRAS}}, \tag{3}$$

where μ labels the catalogue from which the galaxy in question is drawn; each of the four catalogues making up the ORS has its own mean density $\langle n\rangle_\mu$. Here $\langle n\rangle_{\mu,\,IRAS}$ is the mean number density of *IRAS* galaxies in the volume corresponding to the μth catalogue in ORS. This brings each of the subsamples, with their separate selection criteria, to a uniform weighting (Santiago et al. 1996). With the weighting of equation (1) or (3), we can thus calculate the galaxy density *fluctuation field* $\delta(\boldsymbol{x}) \equiv (\rho(\boldsymbol{x}) - \langle\rho\rangle)/\langle\rho\rangle$ throughout the volume surveyed.

For comparison, we also apply our analysis to the complete *IRAS* 1.2-Jy sample (Fisher et al. 1995a; Strauss et al. 1992), which includes 5313 galaxies over 87.6 per cent of the sky. The ZOA in *IRAS* was interpolated according to the Yahil et al. (1991) procedure mentioned above. Hereafter, we refer to this sample as the *IRAS* sample. We note that the ORS and *IRAS* samples are not really independent; roughly 60 per cent of the *IRAS* 1.2-Jy galaxies out to $80\,h^{-1}$ Mpc are also catalogued in the ORS magnitude-limited sample.

We work purely in Local Group redshift space, except in Section 6 on Wiener reconstruction.

3 A BRIEF TOUR OF THE SGP

In this section, we first show the distribution of galaxies in the samples projected on to the various supergalactic planes. We then quantify this by calculating the density field in shells as a function of *SGZ*. Finally, we quantify the centre of mass of the overdensity.

3.1 Visual impression

Historically, the SGP was identified in projected 2D maps. We used the *IRAS* data (which is uniformly sampled over the sky) to revisit the 2D appearance of the SGP by fitting the data to a great circle. For a projected distribution of sources the great circle along which the density of galaxies is enhanced can be found by calculating the covariance matrix: $I_{ij} = \sum_{\rm gal} \hat{x}_i \hat{x}_j$, where the Cartesian axes $\hat{x}_i$ $(i = 1, 2, 3)$ are defined for a unit sphere. The matrix I_{ij} can be diagonalized (cf. Section 4.2) and the smallest eigenvector indicates the direction of the normal to the great circle. We considered the projected *IRAS* galaxy distribution out to 40 and $80\,h^{-1}$ Mpc, and found that the great circle is aligned with the standard de Vaucouleurs' SGP to within 19° and 7°, respectively. Can we see the translation of the great circle to a plane in three dimensions? Fig. 1 shows the distribution of galaxies projected on the sky in the *IRAS* and ORS samples. The distribution is highly non-isotropic, and the SGP is clearly the most prominent feature. We note that the structures seen in ORS and *IRAS* are quite similar, but the ORS map is more densely sampled, and clusters are more prominent. Fig. 2 shows the raw distributions, of ORS and *IRAS* galaxies, uncorrected for selection effects, in a sphere of radius of $40\,h^{-1}$ Mpc projected on the standard (*SGX*–*SGZ*), (*SGX*–*SGY*) and (*SGY*–*SGZ*) planes. The SGP is particularly visible edge-on in the (*SGX*–*SGZ*) and (*SGY*–*SGZ*) projections.

Maps of the smoothed density field, after applying the appropriate weights, are shown elsewhere for the *IRAS* survey (Saunders et al. 1991; Strauss et al. 1992; Fisher et al. 1995b; Strauss & Willick 1995; Webster, Lahav & Fisher 1997) and for ORS (Santiago et al. 1995, 1996; Baker et al. 1998). In Figs 3 and 4 we show histograms of the galaxy density field δ, corrected

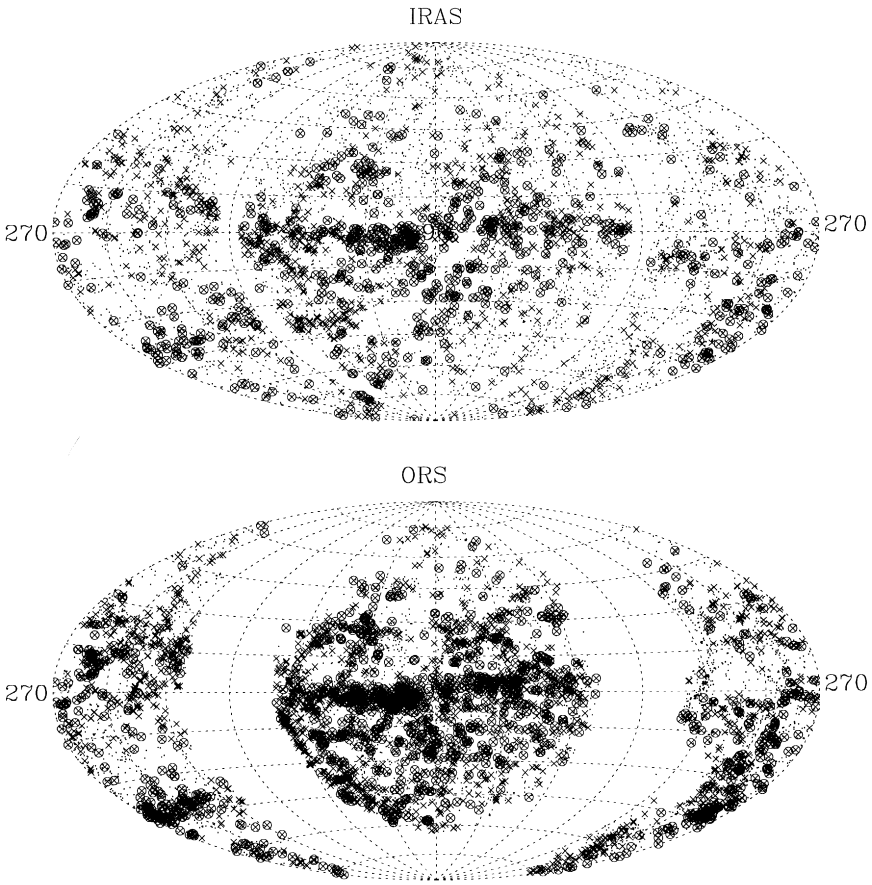

Figure 1. The distribution of galaxies projected on the sky in the *IRAS* and ORS samples. This is an Aitoff projection in supergalactic coordinates, with $SGL = 90°$, $SGB = 0$ (close to the Virgo cluster) in the centre of the map. Objects within $2000\,{\rm km\,s^{-1}}$ are shown as circled crosses; objects between 2000 and $4000\,{\rm km\,s^{-1}}$ are indicated as crosses, and dots mark the positions of more distant objects. Here we include only catalogued galaxies, which is why the zone of avoidance is so prominent in these two figures.

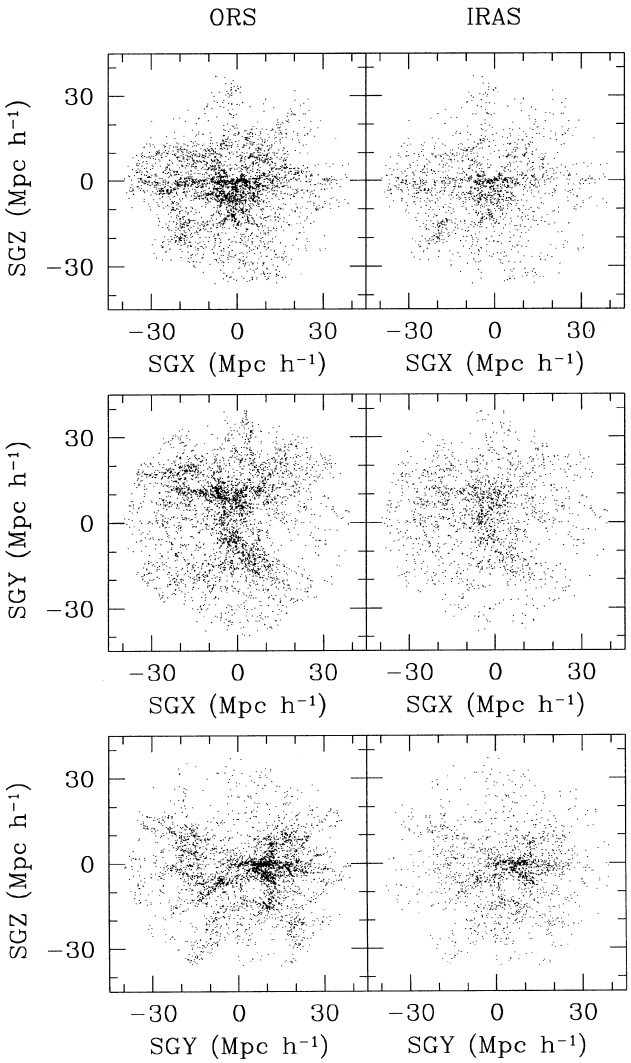

Figure 2. The distributions of ORS and *IRAS* galaxies in a sphere of radius of $40\,h^{-1}$ Mpc, projected on the standard (*SGX*–*SGZ*), (*SGX*–*SGY*) and (*SGY*–*SGZ*) planes. The SGP is visible edge-on as the linear feature at $SGZ = 0$ in the (*SGX*–*SGZ*) and (*SGY*–*SGZ*) projections ORS includes *IRAS* galaxies (real and mock) in the zone of avoidance (see text).

for selection effects, as a function of *SGZ*, averaged over *SGX* and *SGY*, within spheres of ever-larger radii, as indicated in each panel. The SGP is seen as an enhancement at $SGZ = 0$ in these plots to roughly $R_{\rm max} = 60\,h^{-1}$ Mpc, but is not apparent on larger scales.

3.2 The level of overdensity

Our visual impression is that there is indeed a flattened structure in the galaxy distribution, aligned along $SGZ = 0$, extending to appreciable redshifts. To quantify this we calculate the overdensity $\delta_{\rm sgp} \equiv n_{\rm sgp}/\langle n\rangle - 1$ as a function of $R_{\rm max}$, where $n_{\rm sgp}$ is evaluated within a circular cylinder centred on the Local Group with radius $R_{\rm max}$ and height along SGZ of $20\,h^{-1}$ Mpc, and the mean density $\langle n\rangle$ is calculated within a sphere of radius $R_{\rm max}$ (*including* the slab). This overdensity reaches a maximum at $R_{\rm max} = 40\,h^{-1}$ Mpc (for which the volume of the slab is $\sim(46\,h^{-1}\,{\rm Mpc})^3$), $\delta_{\rm sgp}(40) = 0.48 \pm 0.06$ and 0.46 ± 0.09 for ORS and *IRAS*, respectively. At $R_{\rm max} = 60\,h^{-1}$ Mpc, $\delta_{\rm sgp}(60) = 0.36 \pm 0.06$ and 0.26 ± 0.08 for ORS and *IRAS*, respectively. For reference, the rms fluctuations in

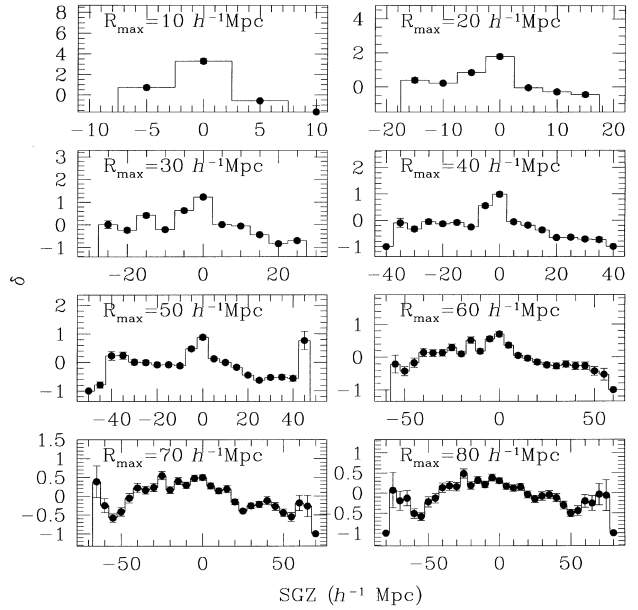

Figure 3. Histograms of the ORS density field (corrected for selection effects) as a function of *SGZ*, averaged over *SGX* and *SGY*, within spheres of radius as indicated in each panel. The binning is $5\,{\rm h}^{-1}$ Mpc. The error bars are Poissonian.

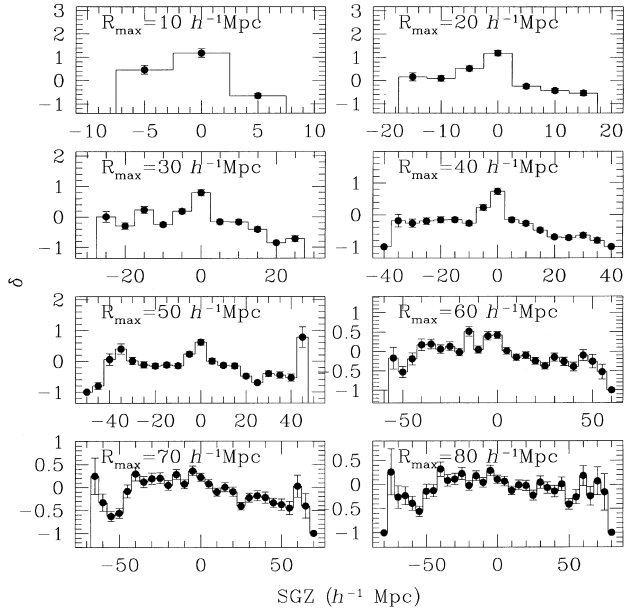

Figure 4. Histograms of the *IRAS* density field (corrected for selection effects) as a function of *SGZ*, averaged over *SGX* and *SGY*, within spheres of radius as indicated in each panel. The error bars are Poissonian.

cubes of volume $(40\,h^{-1}\,{\rm Mpc})^3$ are $\delta_{\rm rms} \sim 0.37$ and ~ 0.30 for optical (Stromlo/APM) and *IRAS* (1.2-Jy) surveys, respectively (Efstathiou 1995). Hence the fluctuation in galaxy counts in a slab aligned with the standard de Vaucouleurs' SGP is no more than $\sim 1.5\sigma$ perturbation on scale of $\sim 40\,h^{-1}$ Mpc. This implies that the SGP is only a modest perturbation on these large scales.

3.3 The centre of the overdensity

In order to quantify the local overdensity, we need to calculate the

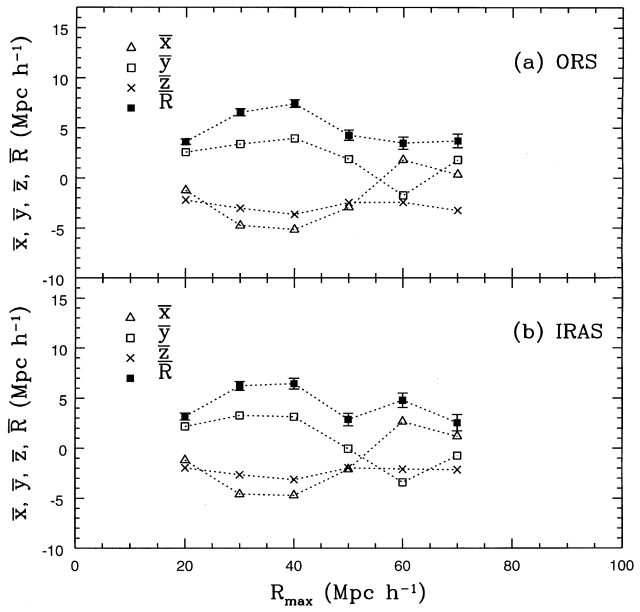

Figure 5. The variation of the mean position of the centre of mass of the galaxy distribution within a sphere of radius $R_{\rm max}$ centred on us, for both the ORS and *IRAS* samples. The curves show the supergalactic x, y, z of the centre of mass, and its radial distance $\bar{R}$ from the origin.

centre of 'mass' of the density field, within a sphere of radius $R_{\rm max}$ centred on us, for both the ORS and *IRAS* samples (cf. Juszkiewicz, Vittorio & Wyse 1990). The centre of mass is given by summing over the galaxies:

$$\bar{x}_i = \frac{1}{V}\sum_{\rm gal} w_{\rm gal} x_i, \tag{4}$$

where $i = 1, 2, 3$, V is the total volume of the sphere of radius $R_{\rm max}$ and $w_{\rm gal}$ is the weight per galaxy described in Section 2. The shot noise error in each axis is

$$\sigma^2_{\bar{x}} = \frac{1}{V^2}\sum_{\rm gal} w^2_{\rm gal}\ x_i^2 = \frac{1}{3V^2}\sum_{\rm gal} w^2_{\rm gal}\ r^2, \tag{5}$$

where the last equality is valid for an isotropic distribution. Fig. 5 shows the coordinates of the centre of the galaxy distribution as a function of $R_{\rm max}$. The centre moves away from the origin (the Local Group) by no more than $8\,h^{-1}$ Mpc for ORS and $6\,h^{-1}$ Mpc for *IRAS*. This is partially due to the 'tug of war' between the Great Attractor and Perseus–Pisces, which largely balance each other out. Indeed, the centre moves back towards the origin for $R_{\rm max} > 40\,h^{-1}$ Mpc. Therefore, we will simply set the centre of mass to the origin in our analyses below.

4 PRINCIPAL COMPONENTS OF THE INERTIA TENSOR

Both visual impression and a formal χ^2 fit suggest that the SGP cannot be fitted by a homogeneous ellipsoid model. We therefore seek a more objective measure of deviation from sphericity, via the moment of inertia tensor (MoI).

4.1 Estimation of the moment of inertia

We can quantify the size, orientation, and extent of the local density by calculating the MoI of the *fluctuation* in the density field (cf. Babul & Starkman 1992; Luo & Vishniac 1995; Dave et al. 1997):

$$\tilde{C}_{ij} = C_{ij} - \bar{C}_{ij} = \frac{1}{\langle n\rangle V}\int [n(\boldsymbol{x}) - n_{\rm bg}](x_i - \bar{x}_i)(x_j - \bar{x}_j)\,{\rm d}V, \tag{6}$$

where $n(\boldsymbol{x})$ is the galaxy number density at position $\boldsymbol{x}$, $\langle n\rangle$ is the mean number density and x_i, x_j $(i, j = 1, 2, 3)$ are Cartesian components of $\boldsymbol{x}$. $\bar{C}$ is the contribution from the uniform background. As we mentioned earlier, as $\bar{\boldsymbol{x}}$ is observed to stay close to zero, we will simply set it to zero in what follows. The integration is over the volume of the sphere. We define the fluctuations in the density field relative to the *background* density $n_{\rm bg}$ in the absence of the slab (which differs from the mean density $\langle n\rangle$ *including* the slab).

For a uniform distribution with density $\langle n\rangle$ the covariance matrix is analytic and isotropic:

$$\bar{C}_{ij} = \frac{f_{\rm bg}}{V}\int x_i x_j\,{\rm d}V = \frac{1}{3}\delta^K_{ij}\frac{f_{\rm bg}}{V}\int_0^{R_{\rm max}} r^2(4\pi r^2\,{\rm d}r) = \delta^K_{ij}\ f_{\rm bg}\frac{R^2_{\rm max}}{5}, \tag{7}$$

where

$$f_{\rm bg} \equiv \frac{n_{\rm bg}}{\langle n\rangle}, \tag{8}$$

$\bar{\boldsymbol{x}}$ is of course zero, and $\delta^{\rm K}_{ij}$ is the Kronecker delta function.

For a discrete density field, such as provided by ORS or *IRAS*, we can calculate the covariance elements by summing over the galaxies:

$$\tilde{C}_{ij} = C_{ij} - \bar{C}_{ij} = \frac{1}{V}\sum_{\rm gal} w_{\rm gal} x_i x_j - \delta^{\rm K}_{ij} f_{\rm bg}\frac{R^2_{\rm max}}{5}. \tag{9}$$

An analytic estimator for Poisson shot-noise per diagonal component of the covariance matrix (assuming no errors in $f_{\rm bg}$) is:

$$\sigma^2_c = \frac{1}{(3V)^2}\sum_{\rm gal} w^2_{\rm gal} r^4. \tag{10}$$

Equation (9) requires knowledge of $f_{\rm bg}$ in order to correct for the background density. However, as the boundaries of the SGP are hard to define a priori and the background will not be uniform, it is difficult to estimate a meaningful $f_{\rm bg}$. In Section 4.3 we suggest a statistic that is independent of this parameter.

4.2 Principal axes

The next step in our analysis is to diagonalize the MoI and find the eigenvalues λ_α and associated eigenvectors $\boldsymbol{u}_\alpha$ $(\alpha = 1, 2, 3)$:

$$\tilde{C}\boldsymbol{u}_\alpha = \lambda_\alpha \boldsymbol{u}_\alpha. \tag{11}$$

The standard deviation ('1σ') along each of the three axes is given by $\sqrt{\lambda_\alpha}$, which we label hereafter as a, b, c. Note that because the background contribution (the last term in equation 9) is isotropic, it only affects the eigenvalues, but not the directions of the eigenvectors. This procedure is essentially the Principal Component Analysis (PCA) – a well-known statistical tool for reducing the dimensionality of parameter space (e.g. Murtagh & Heck 1987 and references therein). By identifying the *linear* combination of input parameters with maximum variance, PCA determines the principal components that can be most effectively used to characterize the input data. In our case, in searching for a plane, we wish to see if the PCA finds one axis to be much shorter than the other two axes.

4.3 Background-independent statistic of axes

Our aim is to quantify deviations from spherical structure. The difficulty in doing so is due to three problems: (i) the background density as modelled above with $f_{\rm bg}$ is ill-determined, (ii) the shot noise owing to the finite number of galaxies can be quite large, and (iii) the distribution of galaxies is distorted owing to peculiar velocities.

We will discuss the shot noise and peculiar-velocity problems in Section 6. To overcome the problem of the unknown background, we can construct the following quantities, which are independent of $f_{\rm bg}$:

$$p^2 = |a^2 - b^2|, \tag{12}$$

$$q^2 = |a^2 - c^2|, \tag{13}$$

and

$$s^2 = |b^2 - c^2|. \tag{14}$$

Note that the (p, q, s) here are in the diagonalized PCA frame, where the axes are ordered by size ($a \geqslant b \geqslant c$). For a perfect sphere, $p = q = s = 0$. For a homogeneous oblate ellipsoid with semimajor axes $A = B > C$, one expects $p = 0$ for all $R_{\rm max}$, but for q and s to increase out to $R_{\rm max} \approx A$ and then to decline. Alternatively, we can calculate (p, q, s) along fixed (x, y, z) axes (e.g. in de Vaucouleurs' system) by replacing a^2, b^2, c^2 in equations (12)–(14) by the non-ordered variances in that fixed coordinate system (i.e. the diagonal elements in the MoI matrix in that (x, y, z) coordinate system).

In the limit that the errors are isotropic, the Poisson error bars are:

$$\Delta p = \sigma_c/p = \Delta(a^2)/p, \tag{15}$$

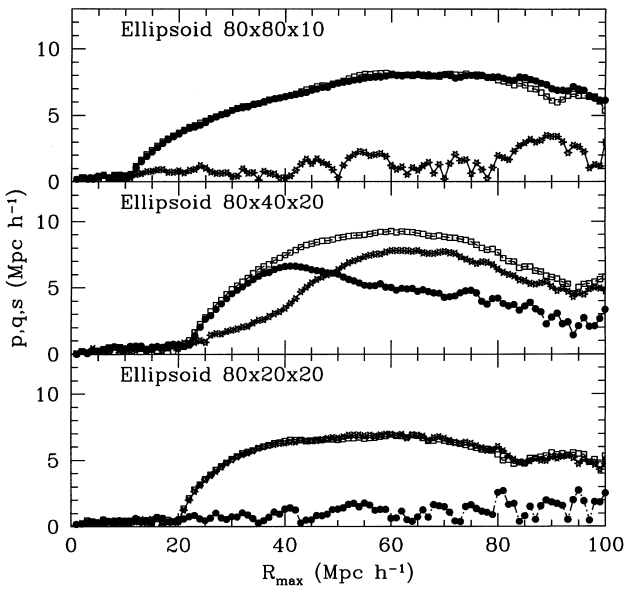

Figure 6. The quantities p (crosses), q (open squares) and s (filled circles) given by equations (12)–(14) versus $R_{\rm max}$ for mock ellipsoids (oblate, prolate and triaxial) with dimensions (in h^{-1} Mpc) indicated in the panels, all ellipsoids with density contrast of $\delta = 0.4$. The mock samples have an *IRAS* selection function, and the results are averaged over 100 realizations at fixed axes. The Poisson scatter can evaluated from equation (15). For example, in the real *IRAS* data we see from Table 1 for $R_{\rm max} = 40$ and $p \sim 10\,h^{-1}$ Mpc, $\Delta p \sim 1\,h^{-1}$ Mpc and for $R_{\rm max} = 80$ and $p \sim 18\,h^{-1}$ Mpc, $\Delta p \sim 2\,h^{-1}$ Mpc. Typical error bars can also be seen in Figs 7, 8, 13 and 14.

and similarly for q and s. We will determine the characteristic shape of the galaxy density field, from the observed p, q and s and their error bars as a function of $R_{\rm max}$. We note that other transformations of (a, b, c) are possible, such as the $(S1, S2, S3)$ statistic proposed by Babul & Starkman (1992).

4.4 Mock realizations

To get an insight into our (p, q, s) statistic we applied it to mock realizations of ellipsoids placed in a uniform background. The *IRAS* selection function was applied to the mock samples, and the results were averaged over 100 realizations. Fig. 6 shows the mean of the quantities p, q, and s over the 100 realizations, derived at fixed axes for mock ellipsoids (oblate, prolate and triaxial) with dimensions indicated in the panels and overdensity of $\delta = 0.4$. When the axes were allowed to be chosen by PCA, the axes agreed with the correct orientation of the ellipsoids to within 7° (rms over 100 realizations). For a single realization the curves are much more noisy (for typical Poission scatter see Table 1), but our

Table 1. SGP parameters from PCA analysis.

$R_{\rm min}$	$R_{\rm max}$	a	b	c	$\Delta(a^2)$	SGL_z	SGB_z
			ORS				
0	20	9.9	8.1	7.1	2.4	160	53
0	30	14.8	12.4	11.0	5.1	173	72
0	40	19.9	16.2	14.3	7.7	104	68
0	50	25.8	20.7	20.0	12.7	76	23
0	60	31.8	26.5	22.7	17.8	67	56
0	70	35.6	31.1	27.0	24.1	48	65
0	80	39.8	35.2	31.0	33.0	58	65
20	40	21.7	17.7	15.4	9.5	101	66
40	60	35.1	29.2	24.8	23.7	65	55
60	80	45.8	40.3	36.2	57.4	52	68
			IRAS				
0	20	10.3	8.1	7.2	3.4	160	62
0	30	14.9	13.0	11.1	6.6	162	71
0	40	19.6	16.8	14.7	10.6	120	75
0	50	25.5	21.3	20.8	16.4	76	−6
0	60	31.2	26.5	23.6	21.9	69	55
0	70	35.1	30.7	27.9	29.3	54	60
0	80	39.6	35.3	32.8	39.0	52	61
20	40	21.3	18.0	15.8	12.8	113	72
40	60	34.2	29.0	25.8	28.8	67	53
60	80	44.9	40.5	38.3	65.9	44	60
			IRAS Wiener				
0	20	10.1	8.5	7.8	–	197	61
0	30	14.6	13.4	11.9	–	176	70
0	40	19.5	17.6	15.9	–	135	75
0	50	24.5	21.4	21.2	–	154	85
0	60	29.7	26.2	24.6	–	72	55
0	70	34.0	30.8	29.0	–	61	60
0	80	38.3	35.3	33.5	–	56	59

Comments on Table 1: $R_{\rm min}$, $R_{\rm max}$, a, b and c are in h^{-1} Mpc. The values of a, b and c are for $f_{\rm bg} = 0$. The Poisson error per axis $\Delta(a^2)$ is derived using equation (10). No errors are given in the Wiener case, as this is a smoothed field (although one can calculate the scatter around the mean).
SGL_z and SGB_z (both in degrees) give the direction in standard de Vaucouleurs' coordinates of the Z component as found by PCA. The angle between this direction and de Vaucouleurs' SGP pole is simply $\theta_z = 90° - SGB_z$.

experiments indicate that the main features can still be seen. When PCA defines the axes, it attempts to maximize the differences between the axes, and the results for p, q and s are biased by noise. For example, in the case of a perfectly oblate structure in the presence of noise, the quantity s increases with radius $R_{\rm max}$, where it is identically zero in the noise-free case. Fortunately, we will see in the following section that the behaviour of (p, q, s) for the real data is quite robust. We will continue these experiments with the mock realizations in Section 7, where we consider more complex geometries.

5 APPLICATION OF MOI TO ORS AND *IRAS*

We now apply the MoI approach to the ORS and *IRAS* samples. We begin by considering p, q and s along *fixed* axes. We will find below that the PCA direction at small $R_{\rm max}$ is indeed very close to that of de Vaucouleurs' system, so we simply choose the standard de Vaucouleurs' SGP axes. Fig. 7 shows p, q and s as a function of $R_{\rm max}$. The most notable feature is the dip in s at about $R_{\rm max} = 50\,h^{-1}$ Mpc in both samples. This is due to the dumbbell-like configuration of Perseus–Pisces and the Great Attractor on opposite sides of the sky. At $R_{\rm max} = 80\,h^{-1}$ Mpc, p tends to small values (in particular in ORS). However, the dramatic changes with $R_{\rm max}$ (in particular at $50\,h^{-1}$ Mpc) call to question the notion of a single coherent feature within the boundaries of our samples (see Section 7). The small value of p at $80\,{\rm h}^{-1}$ Mpc does not necessarily imply that we see a pancake to this limit. Based on Fig. 7, one may argue that the 'plane' terminates at $\sim 40\,h^{-1}$ Mpc.

We now turn to the PCA approach of diagonalizing the MoI derived at each radius $R_{\rm max}$. In this case the axes change direction, and might even 'swap'. 'Swapping' means that an axis that is the largest at a given $R_{\rm max}$ may become say the second or third largest in a different $R_{\rm max}$. We indeed see a discontinuity in the variation of the 'largest' axis at $R_{\rm max} \sim 50\,h^{-1}$ Mpc owing to the Great Attractor and Perseus–Pisces.

The variation at large $R_{\rm max}$ (see Fig. 8) is more difficult to interpret, but we see that $q > p > s$, implying a triaxial shape, and p and q increase with $R_{\rm max}$. In contrast, the toy models (Fig. 6) show that two of $[p, q, s]$ drop with $R_{\rm max}$ beyond the radius that encloses the ellipsoid ($80\,h^{-1}$ Mpc in the toy models). But when comparing Figs 6 and 8, we should keep in mind that at large $R_{\rm max}$ the increase of the observed quantities p, q or s might be due to shot noise. It is also interesting to note the similarity between ORS and *IRAS*, indicating that on the very large scales the density fields in the two samples are quite similar.

Table 1 lists a, b, c, their Poisson errors, and the direction of the PCA Z-component for ORS (for direct summation) and *IRAS* (for both direct summation and Wiener reconstruction described in the next section). Table 1 also lists the values in *differential* shells, showing trends similar to those seen in the cumulative plots.

Figs 9 and 10 show the variation of direction of the PCA Z-component with $R_{\rm max}$. We see that although the angle $\theta_z \equiv 90^\circ - SGB_z$ between the PCA minor axis and de Vaucouleurs' pole is usually less than 30°, there is a significant variation on the sky (relative to the errors of $\sim 10^\circ$ owing to shot noise). Particularly noticeable is the big jump at $R_{\rm max} = 50\,h^{-1}$ Mpc, in accord with the behaviour in Figs 7 and 8. This is again a result of the dumbbell configuration of the Great Attractor and the Perseus–Pisces superclusters, as we shall see in Section 7. Table 1 also gives SGB_z, the complement of the misalignment angle θ_z, for three shells, each $20\,{\rm h}^{-1}$ Mpc wide. We see that

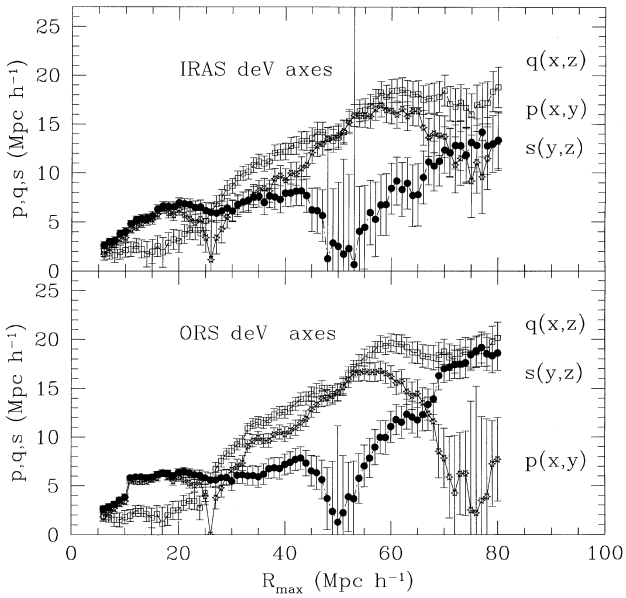

Figure 7. The quantities (p, q, s) derived from the variances along the de Vaucouleurs' axes versus $R_{\rm max}$ (cumulative) for the ORS and *IRAS* samples. The error bars are Poisson.

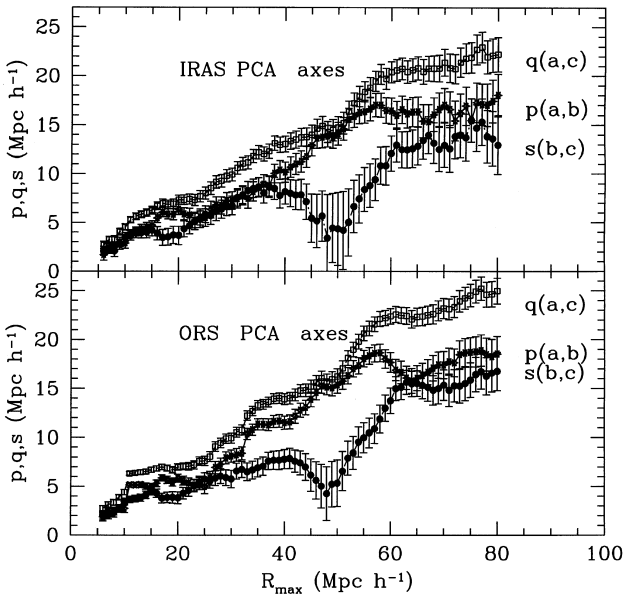

Figure 8. The quantities (p, q, s) derived from PCA dimensions (a, b, c) (equations 12–14) versus $R_{\rm max}$ (cumulative) for the ORS and *IRAS* samples. The error bars are Poisson.

indeed typically $\theta_z \sim 30^\circ$, even at the 60–$80\,{\rm h}^{-1}$ Mpc shell, which is beyond the Great Attractor and Perseus–Pisces. The probability that two random vectors are separated by an angle less than $\theta_z \sim 30^\circ$ by chance is $P(<\theta_z) = [1 - \cos(\theta_z)]$, i.e. ~ 13 per cent.

6 WIENER RECONSTRUCTION

In addition to the problem of shot noise, the density field measured from redshift surveys also suffers from redshift distortions owing to peculiar velocities (see Hamilton 1998 for a review). One approach that deals with both problems is Wiener

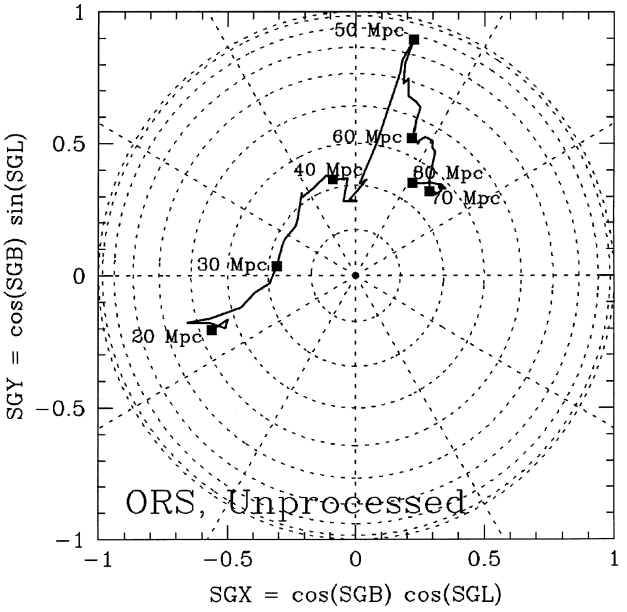

Figure 9. ORS: The direction of the Z axis from the PCA analysis (using direct summation over the galaxies) relative to the de Vaucouleurs' pole. Values of $R_{\rm max}$ are indicated.

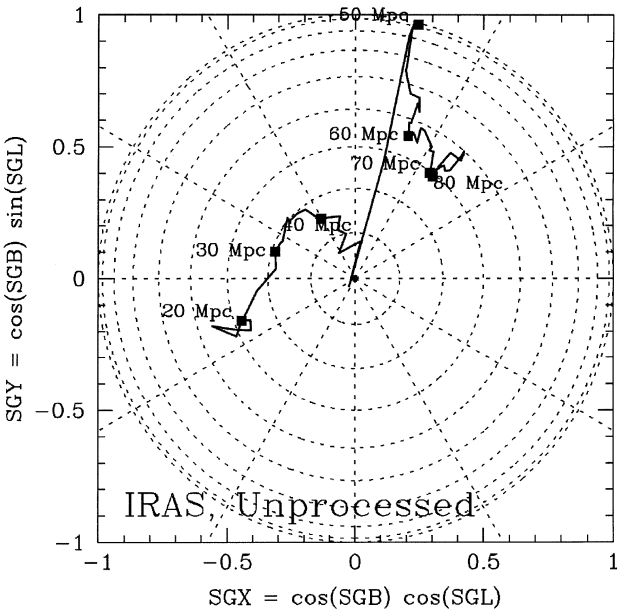

Figure 10. *IRAS*: The direction of the Z axis from the PCA analysis (using direct summation over the galaxies) relative to the de Vaucouleurs' pole. Values of $R_{\rm max}$ are indicated.

filtering (e.g. Lahav et al. 1994; Fisher et al. 1995b). In particular, Fisher et al. (1995b) expand the density field $\delta(\boldsymbol{r})$ in terms of spherical harmonics and Bessel functions. By assuming a prior model for the power spectrum, the coefficients of the expansion can be corrected for the redshift distortion and for the shot noise. This reconstruction is optimal in the minimum-variance sense. In this approach, the smoothed density field approaches the mean density at large distances. This does not mean necessarily that the SGP itself disappears at large distances; it merely reflects our ignorance of the density field where the data are poor.

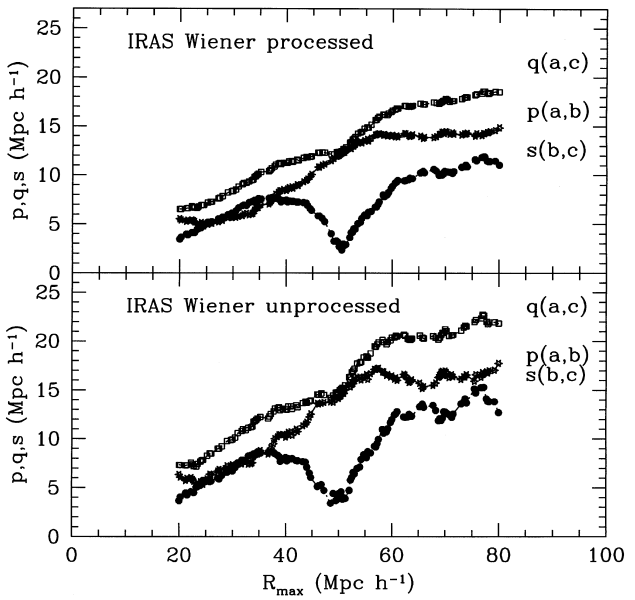

Figure 11. The quantities p, q, s versus $R_{\rm max}$ (cumulative) in PCA axes using spherical harmonic reconstruction of *IRAS* and analytic MoI. Top: corrected for redshift distortion and noise by Wiener filtering, with parameters $\beta = 0.7$, $\Gamma = 0.2$, $\sigma_8 = 0.7$ (reconstruction out to $200\,{\rm h}^{-1}$ Mpc). Bottom: using raw harmonics.

This Wiener approach applied to the density field δ also gives the optimal reconstruction for any property that is linear in δ. In particular, if we seek the optimal reconstruction of the moment of inertia (equation 6) it can be rewritten (for $\bar{\boldsymbol{x}} = 0$) as

$$\tilde{C}_{ij} = \left(\frac{3}{4\pi R_{\rm max}^3}\right) I_{ij} + (1 - f_{\rm bg})\frac{R^2}{5}\delta_{ij}^{\rm K}, \tag{16}$$

where

$$I_{ij} = \int_R \delta(\boldsymbol{r}) x_i x_j \, {\rm d}V. \tag{17}$$

Webster, Lahav & Fisher (1997) give analytic expressions for I_{ij} in terms of the reconstructed coefficients δ_{lmn}^R, and show that only harmonic modes $l = 0$ and $l = 2$ contribute.

We apply this technique below to the reconstructed, real-space density field of *IRAS* galaxies, assuming as priors $\beta \equiv \Omega^{0.6}/b = 0.7$, normalization $\sigma_8 = 0.7$ and a CDM power spectrum with shape parameter $\Gamma = 0.2$.

Fig. 11 shows p, q and s for *IRAS* before and after Wiener filtering in spherical harmonic presentation. Fig. 12 shows the variation of the minor PCA axis with $R_{\rm max}$. There is good agreement with the results of direct summation shown in Fig. 8, indicating that shot noise and redshift distortion do not introduce big systematic effects in our statistics. Unfortunately, the Wiener procedure cannot easily be applied to the ORS sample, as it only covers $|b| > 20°$.

7 INTERPRETATION OF THE MOI RESULTS

The behaviour of the MoI axes for both ORS and *IRAS* indicate that the SGP is a structure far more complicated than a homogeneous ellipsoid or a slab. In the local universe, there is 'contamination' owing to clusters and voids below and above the SGP. To get further insight to the structure that generates the

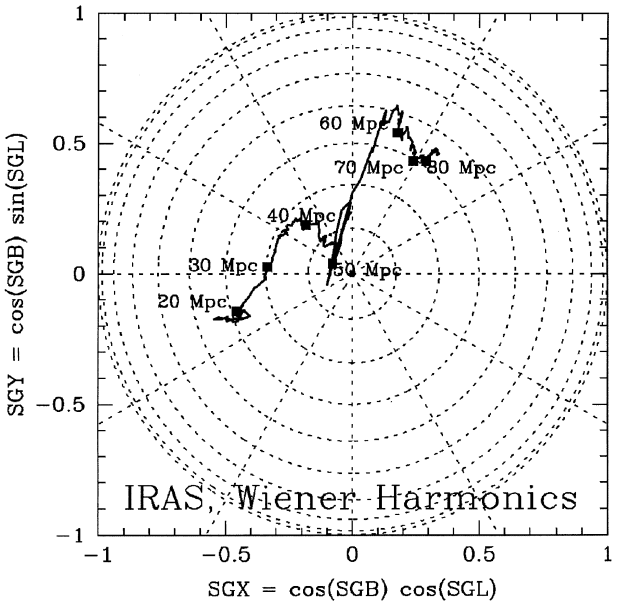

Figure 12. Wiener filtering of *IRAS*: The direction of the Z axis (as found by PCA) relative to the de Vaucouleurs' pole. Values of $R_{\max}$ are indicated.

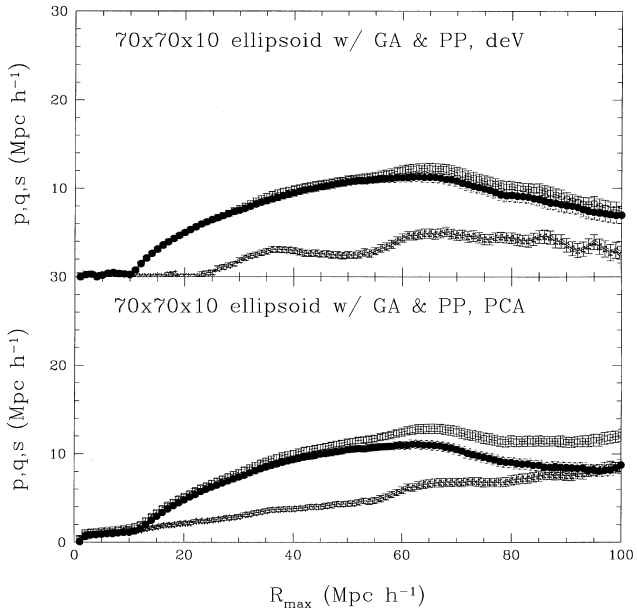

Figure 13. The quantities p, q, s versus $R_{\max}$ (cumulative) in fixed and PCA axes for a mock realizations of an oblate ellipsoid of $40\times40\times10(h^{-1}\,\mathrm{Mpc})^3$ plus two clusters (PP and GA), as described in the text. The upper panel uses fixed supergalactic coordinates, while the lower panel uses the axes found by the PCA analysis. The curves show the mean and errors from 100 ORS-like realizations.

observed MoI, we generated mock realizations of ORS-like sample with more complicated geometries than the simple ellipsoids used in Section 4.4, trying to mimic the significant overdensities seen in the real universe. In particular, we put in: (i) an ellipsoid with dimensions of $40\times40\times10(h^{-1}\,\mathrm{Mpc})^3$ and overdensity $\delta=1$ aligned with the supergalactic plane, (ii) a sphere of radius $11\,h^{-1}$ Mpc and overdensity $\delta=3$, representing a Perseus–Pisces-like supercluster at $(SGX, SGY, SGZ) = (49, -23, 0)\ h^{-1}$ Mpc, and (iii) a sphere of radius $10\,h^{-1}$ Mpc and overdensity $\delta=3$, representing a Great Attractor-like structure at $(SGX, SGY, SGZ) = (-32, 0, 0)\,h^{-1}$ Mpc.

Fig. 13 shows (p,q,s) averaged over 100 realizations in fixed and PCA coordinates. In Fig. 14 we show a similar mock configuration, but for an ellipsoid of $70\times70\times10(h^{-1}\,\mathrm{Mpc})^3$, with the aim of assessing if the SGP continues beyond $R_{\max}=40\,h^{-1}$ Mpc.

It is interesting to contrast Figs 13 and 14 with Figs 7, 8 and 11 obtained for the real ORS and *IRAS* data. First, the behaviour of p, q and s in the mock realizations is more gentle than in the real data. For example, we see that the dip in s at $R_{\max}\sim50\,h^{-1}$ Mpc in the real data is only marginally reproduced in the toy models. Secondly, while it is easy to distinguish in Figs 13 and 14 between 40 and $70\,h^{-1}$ Mpc ellipsoids, the behaviour of p, q and s in the real data is more ambiguous. However, in the real data we see no decline in p and q up to at least $R_{\max}\sim60\,h^{-1}$ Mpc. We note that the toy models in Figs 13 and 14 do not reproduce the observed growth of p, q and s on large scales, which might be the result of shot noise. But these toy examples illustrate that the observed behaviour of p, q and s can be accounted for by adding few major superclusters to a pancake-like structure.

We note that recent simulations for a variety of models (e.g. Bond et al. 1996; Jenkins et al. 1998) show a web of filaments and sheets, with 'knots' at their intersection, or alternatively, 'arms stretching from clusters'. It may well be that Perseus–Pisces and the Great Attractor represent such knots. Hence the MoI 'shape-finder' statistic, when applied to many points in space, could be an efficient way of detecting such patterns and discriminating between models.

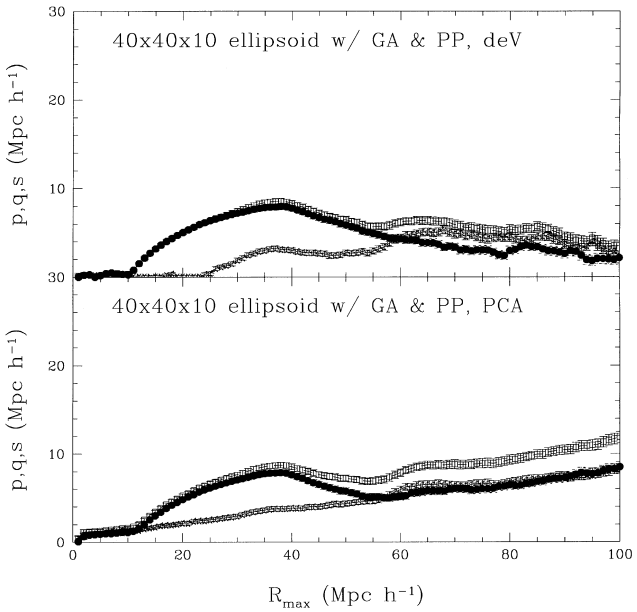

Figure 14. The quantities p, q, s versus $R_{\max}$ (cumulative) in fixed and PCA axes for a mock realizations of an oblate ellipsoid of $70\times70\times10(h^{-1}\,\mathrm{Mpc})^3$ plus two clusters (PP and GA), as described in the text. The upper panel uses fixed supergalactic coordinates, while the lower panel uses the axes found by the PCA analysis. The curves show the mean and errors from 100 ORS-like realizations.

8 CONCLUSIONS

We have presented a moment of inertia approach to study the existence and extent of the planar structure in the local galaxy density field, the supergalactic plane (SGP).

Our main conclusions from the present analysis are:

(i) The SGP is not well-modelled as a homogeneous ellipsoid.

(ii) The moments of inertia analysis of the galaxy density field shows that the normal to the plane is within $\theta_z \sim 30°$ of the standard SGP *Z*-axis, out to a radius of $80\,h^{-1}$ Mpc, for both ORS and *IRAS*. However, the normal changes direction with $R_{\max}$, in particular at $\sim 50\,h^{-1}$ Mpc, owing to the presence of Perseus–Pisces and the Great Attractor. The shape too varies with $R_{\max}$, and in fact at $50\,h^{-1}$ Mpc the SGP looks more like a dumbbell than a pancake. Based on Figs 7, 8 and 11 one may argue that the 'plane' terminates at $\sim 40\,h^{-1}$ Mpc. However, we note that the axes of the shell $60–80\,h^{-1}$ Mpc are aligned with the standard SGP to within 30°.

(iii) The density contrast in the slab with $R_{\max} = 40\,h^{-1}$ Mpc and thickness of $20\,h^{-1}$ Mpc centred on the Local Group and aligned along the supergalactic axes is $\delta_{\rm sgp} \sim 0.5$ for both ORS and *IRAS*.

(iv) The SGP axes and density contrast are similar for both ORS and *IRAS*. In other words, the relative biasing optical-to-*IRAS* is nearly unity on the $\sim 40\,h^{-1}$ Mpc scales (while it is known to be somewhat larger than 1 on $< 10\,h^{-1}$ Mpc scales).

(v) An optimal minimum variance reconstruction (Wiener filtering in spherical harmonics representation), which corrects *IRAS* for both redshift distortion and shot noise, yields similar misalignment of angle and axes.

(vi) It may well be that Perseus–Pisces and the Great Attractor represent 'knots' in a web of filaments and sheets, as seen in recent *N*-body simulations. This complicated structure calls to question the notion of a single coherent feature on Gpc scales (as claimed e.g. by Tully 1986, 1987), and the possible connectivity between the Great Attractor and the Shapley supercluster at $\sim 140\,h^{-1}$ Mpc (e.g. Scaramella et al. 1992).

Regarding the wider cosmological implications, the present analysis is as an example of applying the MoI at only one point, centred at us. It is of interest to compare the SGP to other structures, e.g. the Great Walls seen in the CfA and SSRS surveys. One can calculate moments of inertia at many points in space and contrast the statistical behaviour of the axes with *N*-body simulations. Results from volume limited subsets of *N*-body simulations show indeed that the MoI statistic quantifies, e.g. differences in filamentary structure between cold and hot dark matter models (e.g. Dave et al. 1997; Webster 1998). Unfortunately, the flux limited ORS and *IRAS* catalogues are too shallow to apply the statistic in other points in space. Volume-limited subsets from new large redshift surveys [e.g. 2dF (Colless 1998) and SDSS (Gunn & Weinberg 1995)] would be suitable for such shape-finding algorithms.

It also is possible to improve the above analysis by calculating the moment of inertia for a pre-selected high-density region. This can be done by methods such as minimal-spanning-trees or percolation (which can practically be applied only to volume-limited samples), or by considering a smoothed density field and defining a certain density threshold. It would also be interesting to repeat the analysis for different morphological types and weighting schemes; for example, by calculating luminosity-weighted, rather than number-weighted, galaxy counts. On the statistical side, other more general shape-finders can be applied, e.g. by utilizing the Minkowski functions (e.g. Mecke, Buchert & Wagner 1994; Sahni, Sathyaprakash & Shandarin 1998).

ACKNOWLEDGMENTS

We thank J. Bagla, A. Dekel, K. Fisher, D. Lynden-Bell, P. Monaco and S. Shandarin for helpful discussions and the referee for useful comments. MD acknowledges support from NSF grant AST95-28340. JPH was supported by the Smithsonian Institution and NASA NAGW-201. OL thanks the Weizmann Institute (Israel), the Ango-Australian Observatory and ATNF/CSIRO (Australia) for their hospitality. MAS acknowledges support from the Alfred P. Sloan Foundation, Research Corporation, and NSF grant AST96-16901. AMW acknowledges the receipt of a PPARC studentship.

REFERENCES

Babul A., Starkman G. D., 1992, ApJ, 401, 28
Bahcall N., 1988, ARA&A, 26, 631
Baker J. E., Davis M., Strauss M. A., Lahav O., Santiago B. X., 1998, ApJ, 508, 6
Baleisis A., Lahav O., Loan A. J., Wall J. V., 1998, MNRAS, 297, 545
Bardeen J. M., Bond J. R., Kaiser N., Szalay A., 1986, ApJ, 304, 15
Bond R., Kofman L., Pogosyan D., 1996, Nat, 380, 606
Colless M., 1998, Phil. Trans. R. Soc. Lond. A, in press (astro-ph/9804079)
Corwin H. G., Skiff B. A., 1995, Extension to the Southern Galaxies Catalogue, in electronic form
Dave R., Hellinger D., Primack J., Nolthenius R., Klypin A., 1997, MNRAS, 284, 607
Davis M., Huchra J. P., 1982, ApJ, 254, 437
de Vaucouleurs G., 1953, AJ, 58, 30
de Vaucouleurs G., 1956, Vistas Astron., 2, 1584
de Vaucouleurs G., 1958, ApJ, 63, 223
de Vaucouleurs G., 1975a, ApJ, 202, 610
de Vaucouleurs G., 1975b, ApJ, 202, 616
de Vaucouleurs G., de Vaucouleurs A., Corwin H. G., Jr, 1976, The Second Catalogue of Bright Galaxies. University of Texas Press, Austin
de Vaucouleurs G., de Vaucouleurs A., Corwin H. G. Jr, Buta R., Paturel G., Fenque P., 1991, The Third Catalogue of Bright Galaxies (RC3). University of Texas Press, Austin
Di Nella H., Paturel G., 1995, Publ. Astron. Soc. Aust., 12, 26
Doroshkevich A. G., 1970, Afz, 6, 320
Efstathiou G., 1995, in Schaefer R., ed., Les Houches Lectures. Elsevier Science, Amsterdam, p. 133
Fisher K. B., Huchra J. P., Davis M., Yahil A., Schlegel D., 1995a, ApJS, 100, 69
Fisher K. B., Lahav O., Hoffman Y., Zaroubi S., Lynden-Bell D., 1995b, MNRAS, 272, 885
Flin P., 1986, Acta Cosmologica, 14, 7
Gunn J. E., Weinberg D. H., 1995, in Maddox S. J., Aragón-Salamanca A., eds, Wide-Field Spectroscopy and the Distant Universe. World Scientific, Singapore, p. 3
Hamilton A. J. S., 1998, in Hamilton D., ed., Ringberg Workshop on Large-Scale Structure. Kluwer, Amsterdam, p. 185
Hermit S., Santiago B. X., Lahav O., Strauss M. A., Davis M., Dressler A., Huchra J. P., 1996, MNRAS, 283, 709
Hoffman G. L., Salpeter E. E., 1982, ApJ, 263, 485
Jenkins A. et al., 1998, ApJ, 499, 20
Juszkiewicz R., Vittorio N., Wyse R. F. G., 1990, ApJ, 349, 408
Lahav O., Fisher K. B., Hoffman Y., Scharf C. A., Zaroubi S., 1994, ApJ, 423, L93
Lauberts A., 1982, The ESO/Uppsala Survey of the ESO(B) Atlas. European Southern Observatory, Munich
Lilje P., Yahil A., Jones B., 1986, ApJ, 307, L91
Lin C. C., Mestel L., Shu F. H., 1965, ApJ, 142, 1431
Loan A. J., 1997, PhD thesis, Cambridge University
Luo S., Vishniac E., 1995, ApJS, 96, 429
Lynden-Bell D., 1988, in Lahav O., Rubin V. C., Coyne G. V., eds, Large-Scale Motions in the Universe: A Vatican Study Week. Princeton University Press, Princeton, p. 199

Lynden-Bell D., Faber S. M., Burstein D., Davies R. L., Dressler A., Terlevich R. J., Wegner G., 1988, ApJ, 326, 19
Mecke K. R., Buchert T., Wagner H., 1994, A&A, 288, 697
Murtagh F., Heck A., 1987, Multivariate Data Analysis. Reidel, Dordrecht
Nilson P., 1973, The Uppsala General Catalogue of Galaxies. Ann. Uppsala Astron. Obs. Band 6, Ser. V:A. Vol 1
Raychaudhury S., 1989, PhD thesis, Cambridge University
Rubin V., 1951, AJ, 56, 47
Rubin V., 1989, in The World of Galaxies. Springer-Verlag, New York, p. 431
Sahni V., Sathyaprakash B. S., Shandarin S. F., 1998, ApJ, 495, L5
Santiago B. X., Strauss M. A., Lahav O., Davis M., Dressler A., Huchra J. P., 1995, ApJ, 446, 457
Santiago B. X., Strauss M. A., Lahav O., Davis M., Dressler A., Huchra J. P., 1996, ApJ, 461, 38
Sathyaprakash B. S., Sahni V., Shandarin S. F., Fisher K. B., 1998, ApJ, 507, L109
Saunders W. et al., 1991, Nat, 349, 32
Scaramella R., 1992, ApJ, 390, L57
Shaver P. A., Pierre M., 1989, A&A, 220, 35
Stanev T., Biermann P. L., Lloyd-Evans J., Rachen J. P., Watson A., 1995, Phys. Rev. Lett., 75, 3056
Strauss M. A., Willick J. A., 1995, Phys. Rep., 261, 271
Strauss M. A., Yahil A., Davis M., Huchra J. P., Fisher K. B., 1992, ApJ, 397, 395
Tully B. R., 1986, ApJ, 303, 25
Tully B. R., 1987, ApJ, 323, 1
Tully B. R., Shaya E., 1984, ApJ, 281, 56
Waxman E., Fisher K. B., Piran T., 1997, ApJ, 483, 1
Webster A. M., 1998, PhD thesis, Cambridge University
Webster A. M., Lahav O., Fisher K. B., 1997, MNRAS, 287, 425
White S. D. M., Silk J., 1979, ApJ, 231, 1
Yahil A., Strauss M. A., Davis M., Huchra J. P., 1991, ApJ, 372, 380
Zel'dovich Y. B., 1970, A&A, 5, 84

This paper has been typeset from a TEX/LATEX file prepared by the author.